REPORT DOCUMENTATION PAGE

Form Approved
OMB No. 0704-0188

1. REPORT DATE *(DD-MM-YYYY)*	2. REPORT TYPE	3. DATES COVERED *(From - To)*
06/29/2006	Final	1 April 2003- 30 March 2006

4. TITLE AND SUBTITLE
Coherent Structures and Chaos Control in High-Power Microwave Devices

5a. CONTRACT NUMBER

5b. GRANT NUMBER
F49620-03-1-0230

5c. PROGRAM ELEMENT NUMBER

6. AUTHOR(S)
Chiping Chen

5d. PROJECT NUMBER

5e. TASK NUMBER

5f. WORK UNIT NUMBER

7. PERFORMING ORGANIZATION NAME(S) AND ADDRESS(ES)
Massachusetts Institute of Technology
Cambridge, MA 02139
Kensington, MD 20895

8. PERFORMING ORGANIZATION REPORT NUMBER

9. SPONSORING/MONITORING AGENCY NAME(S) AND ADDRESS(ES)
Air Force Office of Scientific Research
4015 Wilson Blvd
Mail Room 713
Arlington, VA 22203

10. SPONSOR/MONITOR'S ACRONYM(S)
AFOSR

11. SPONSOR/MONITOR'S REPORT NUMBER(S)
AFRL-SR-AR-TR-06-0290

12. DISTRIBUTION/AVAILABILITY STATEMENT
Distribution A; distribution unlimited

Dr Nachman/NM

13. SUPPLEMENTARY NOTES

14. ABSTRACT

This report summarizes research results obtained under the auspices of Air Force of Scientific Research, Grant No. F49620-03-1-0230 (Chen, 2003). In particular, we conducted vigorous theoretical and computational investigations of coherent structures and chaos in a wide range of intense electron beam plasmas relevant to the development of high-power microwave sources for directed energy applications. The following is a brief summary of our research accomplishments in selected areas, while detailed findings are described in the preprints cited in this report.

15. SUBJECT TERMS

20060727323

16. SECURITY CLASSIFICATION OF:			17. LIMITATION OF ABSTRACT	18. NUMBER OF PAGES	19a. NAME OF RESPONSIBLE PERSON
a. REPORT	b. ABSTRACT	c. THIS PAGE			19b. TELEPHONE NUMBER *(Include area code)*
U	U	U	UU		

Final Report

Coherent Structures and Chaos Control in High-Power Microwave Devices

AFOSR Grant No. F49620-03-1-0230

Submitted to:
Dr. Arje Nachman
Program Manager
Air Force Office of Scientific Research
875 North Randolph Road
Suite 325, Room 3112
Arlington, VA 22203
Phone: 703-696-8427
FAX: 703-696-8450

Submitted by
Plasma Science and Fusion Center
Massachusetts Institute of Technology
Cambridge, Massachusetts 02139

Principal Investigator
Dr. Chiping Chen

Grant Period
April 1, 2003 – March 30, 2006

Table of Contents

Final Report
Coherent Structures and Chaos Control in High-Power Microwave Devices
AFOSR Grant No. F49620-03-1-0230

This report summarizes research results obtained under the auspices of Air Force of Scientific Research, Grant No. F49620-03-1-0230 (Chen, 2003). In particular, we conducted vigorous theoretical and computational investigations of coherent structures and chaos in a wide range of intense electron beam plasmas relevant to the development of high-power microwave sources for directed energy applications.

The following is a brief summary of our research accomplishments in selected areas, while detailed findings are described in the preprints cited in this report.

1. High-Power Magnetron Research

Under the auspices of the present grant (Chen, 2003), we developed equilibrium theories of electron flow in magnetrons and crossed field devices, taking into account the influence of the corrugation on the anode on the electron flow properties. Under certain conditions, both theories predicted the existence of vortex structures induced by the corrugation on the anode (Davies and Chen, 2006; Bhatt and Chen, 2003 and 2004). Vortex formation is a new phenomenon which had not been discussed in the literature in the context of magnetrons and crossed field devices. Since the report of vortex formation (Chen, 2004) at Magnetron/PIC Simulation Workshop held at AFRL, May 2-3, 2004, several researchers at AFRL (Cartwright, 2005) and elsewhere (Bosman, et al., 2005) are exploring use of non-axisymmetric cathodes to improve magnetron performance.

We also formulated a small-signal gain theory for magnetrons (Chen, 2005), using both the Floquet theorem and the Maxwell equations. Once it is fully developed, it will advance the existing magnetron gain theories (Riyopoulos, 1998; Kaup, 2005, and references therein) which do not include them simultaneously.

1.1. Discovery of Vortex Structures in Magnetrons (Davies and Chen, 2006; Bhatt and Chen, 2003 and 2004)

Until our work (Davies and Chen, 2006, Bhatt and Chen, 2003 and 2005), the influence of the anode corrugation on the equilibrium electron flow properties had not been discussed in the magnetron literature. In fact, all conventional treatments of the equilibrium electron flows in magnetrons had ignored effects of the corrugations at the anode (see, for example, Davidson, et al., 1991).

We developed two equilibrium theories to describe the equilibrium electron flow in magnetrons and crossed field devices. One of the equilibrium theories was based on a guiding-center model in which the electron flow velocity is given by the $\mathbf{E}\times\mathbf{B}$ drift velocity (Davies and Chen, 2006). The other was a general treatment in which the electron flow velocity is determined from the cold-fluid force equation (Bhatt and Chen, 2003 and 2004). Both theories predicted the formation of periodic vortex structures in the equilibrium electron flow.

By definition, an equilibrium flow corresponds to a state in magnetrons and crossed-field devices in the absence of rf oscillations. While it is an ideal situation in an actual

device, it is of critical importance in order for us to develop a better understanding of magnetrons and crossed-field devices.

1.1.1. Guiding-Center Theory (Davies and Chen, 2006)

We have made an analysis of non-axisymmetric $\mathbf{E}\times\mathbf{B}$ equilibrium flow in a crossed-field apparatus (Davies and Chen, 2006). The apparatus consists of a conducting circular-cylindrical cathode encompassed by either a corrugated conducting anode or by a periodically biased, circular-cylindrical wall. A uniform magnetic field is directed parallel to the cathode axis. With the aid of perturbation theory, the guiding-center approximation, and the assumption of a constant electron density in the electron layer, we determine equipotential surfaces, electron trajectories, and the corrugated boundary of the electron layer.

An interesting result is the appearance of vortex structures in regions of negative potential near the cathode surface. The scaling properties of the width and potential depth of the vortex are studied for the small-amplitude corrugation regime. For sufficiently thin electron layers, results are shown to be applicable to relatively high density regimes as well as to low density regimes.

While detailed results of this research are described in the manuscript "Vortex structure in a high-density non-axisymmetric $\mathbf{E}\times\mathbf{B}$ equilibrium flow" by J.A. Davies and C. Chen at the appendix of this report, we highlight below some the key features of the vortex structures.

Figure 1.1 shows a schematic of a magnetron in a two-dimensional configuration, where the corrugated anode corresponds to an equipotential surface. Rather than designing the anode corrugations to achieve desired electromagnetic properties in an actual device in the conventional design practice, we determine the corrugated anode self-consistently from the theory, as an *inverse* problem. Because there is considerable freedom for us to choose the anode within our theory, we can fine-tune the corrugated anode give us the desired electromagnetic properties in magnetron design.

Figure 1.2 shows the equilibrium electron flow for the case of a uniform density profile extending from the cathode to the periodic electron layer boundary. In Fig. 1.2, the normalization is chosen as $\rho = r/a$ and $\zeta = \phi/4\pi n_0 e a^2$, where a is the cathode radius, $-e$ is the electron charge, ϕ is the electrostatic potential, and n_0 is the electron density. The cathode is at $\rho - 1 = 0$, whereas the anode is at $\zeta = \zeta_A = 0.03$. The solid curve with $\zeta = 0.00301$ represents the electron layer boundary. Electrons move along the equipotential curves. The close-up shows one of 6 vortices near the cathode.

In general, vortex structures form near the space-charge-limited emission condition, which, in our theory, corresponds to the condition that the radial electric field averaged over the azimuthal angle vanishes at the cathode.

We have also shown that vortex structures occur when the electron density is non-uniform, which will be a subject of our second paper on vortex structures in the equilibrium electron flow in magnetrons and crossed-field devices.

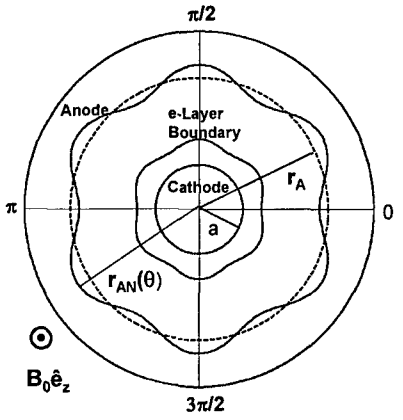

Figure 1.1: Schematic of a magnetron in a two-dimensional configuration. The cathode is located at $r = a$, whereas the corrugated anode is at $r = r_{AN}(\theta)$. The electron layer, which extends from the cathode to the e-layer boundary, is confined by the applied magnetic field $B_0\hat{\mathbf{e}}_z$ (from Davies and Chen, 2006).

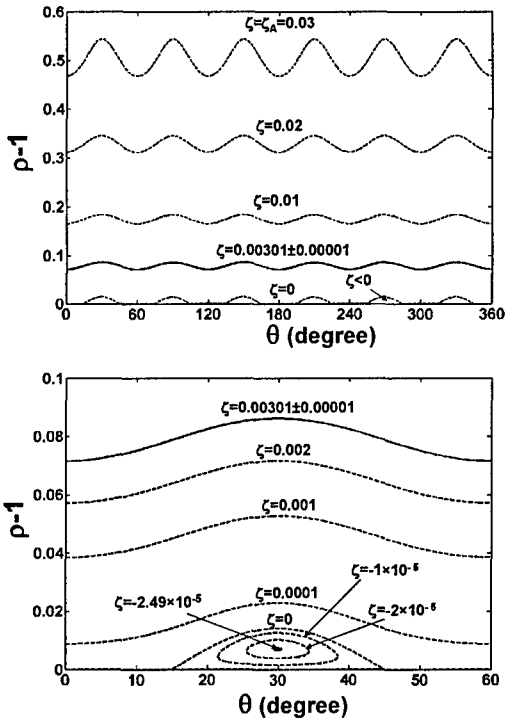

Figure 1.2: Equipotential curves in the equilibrium electron flow (top) and their close-up (bottom). The cathode is at $\rho - 1 = 0$, whereas the anode is at $\zeta = \zeta_A = 0.03$. The solid curve with $\zeta = 0.00301$ represents the electron layer boundary. Electrons move along the equipotential curves. The close-up shows one of 6 vortices near the cathode (from Davies and Chen, 2006).

1.1.2. Cold-Fluid Theory (Bhatt and Chen, 2003 and 2004)

The guiding-center model discussed in Sec. 1.1.1 is applicable to non-relativistic magnetrons and crossed-field devices with thin electron layers, i.e., $r/a-1<<1$. We also investigated vortex structures in the equilibrium using a cold-fluid model. In the cold-fluid model, the restriction $r/a-1<<1$ was removed.

Because the electron flow velocity is given by the cold-fluid force balance equation rather than the simple $\mathbf{E}\times\mathbf{B}$ drift (which is incompressible flow, i.e., divergence-free flow), the electron motion is considerably more complicated, in general. The problem is still tractable.

In particular, we solved the 2D cold-fluid equations by introducing a generalized boundary-conformal coordinate system and scalars representing curl-free and divergence-free velocity fields. The cold-fluid equations are:

$$0=\left(\omega_c+\nabla^2\Psi\right)\nabla^2\Phi+\nabla\left(\nabla^2\Psi\right)\cdot\nabla\Phi+\hat{\mathbf{e}}_z\cdot\left[\nabla\Psi\times\nabla\left(\nabla^2\Psi\right)\right] \tag{1.1}$$

and

$$0=\left(\nabla^2\Phi+\mathbf{V}\cdot\nabla\right)\left\{\frac{1}{2}\nabla^2\mathbf{V}^2-\left(\omega_c+\nabla^2\Psi\right)\nabla^2\Psi-\nabla\left(\nabla^2\Psi\right)\cdot\nabla\Psi-\hat{\mathbf{e}}_z\cdot\left[\nabla\left(\nabla^2\Psi\right)\times\nabla\Phi\right]\right\} \tag{1.2}$$

where $\mathbf{V}=\nabla\Phi+\hat{\mathbf{e}}_z\times\nabla\Psi$ and $\omega_c=qB/mc$.

For a uniform magnetic field and uniform energy profile across the fluid, we found that $\nabla^2\Psi=-\omega_c=\text{const}$, which corresponds to a generalization of Brilliouin flow (Davidson, 1990). In this situation, the 2D cold-fluid equations reduce to a single nonlinear partial differential equation, i.e.,

$$0=\left[\nabla^2\Phi+\left(\nabla\Phi+\hat{\mathbf{e}}_z\times\nabla\Psi\right)\cdot\nabla\right]\nabla^2\left[\left(\nabla\Psi\right)^2+\left(\nabla\Phi\right)^2+2\hat{\mathbf{e}}_z\cdot\left(\nabla\Psi\times\nabla\Phi\right)\right]. \tag{1.3}$$

For small departures of the electron flow from azimuthal symmetry, we solved the nonlinear equation (1.3) perturbatively.

As an example, we considered a simple case where the inner boundary of the electron layer is azimuthally symmetric. In terms of units normalized to this inner radius, we represented this surface by $r=a(\theta)=1$. On the outer boundary of the electron layer, we introduced a small ripple, describing it by $r=b(\theta)=1.8\times\left[1+0.01\cos(2\theta)\right]$. Solving for the fluid flow in this thick annulus, we found areas where the velocity field reverses on itself, forming fluid vortices as shown in Fig. 1.3. These vortices are also regions of potential minima, providing opportunities for ion trapping and the associated noise mechanisms (Yamamoto, et al., 1987).

Our discovery of vortex structures in magnetrons and crossed-field amplifiers provides new insight into a number of areas in magnetron and CFA research, including

a) Elimination of ion trapping and ion noise,
b) Elimination of turbulence and noise,
c) Improvement of magnetron efficiency (Cartwright, 2005), and

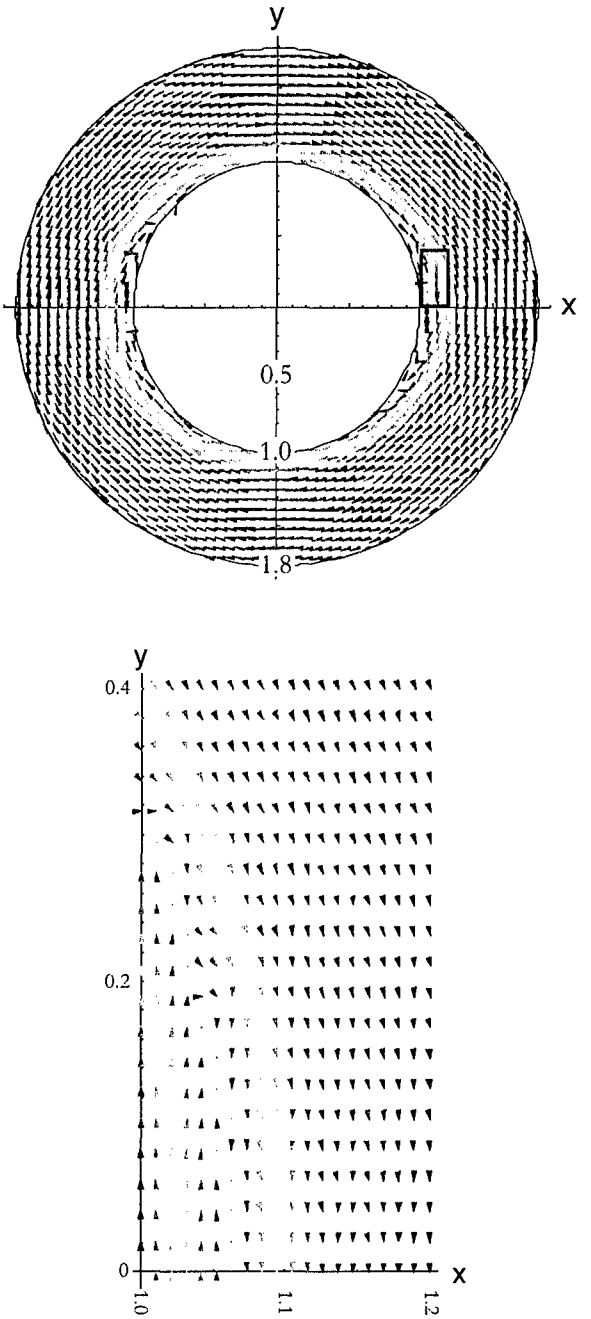

Figure 1.3: Vector field plots of the flow velocity as computed from the perturbation theory for a small ripple on the outer fluid boundary surface. Color indicates the magnitude of the fluid velocity at a given location. Shown on the top is the entire annulus. A close up of the rectangular region on the annulus (bottom) reveals a portion of a vortex centered at $x = 1.06$ and $y = 0$ (from Bhatt and Chen, 2003).

d) Suppression of mode competition (Bosman, et al, 2005).

Some of these items will be the subject of our future investigations.

1.2. Formulation of Small-Signal Gain Theory of Multiresonator Cylindrical Magnetrons (Chen, 2005)

We formulated a small-signal gain theory of magnetrons for a muliresonator cylindrical magnetron (Fig. 1.4) using the linearized cold-fluid equations, the full Maxwell equations, and the Floquet theorem. The gain equation is expressed as an eigenvalue problem defined by (Chen, 2005)

$$\frac{1}{r}\frac{d}{dr}\left[\frac{r}{1-\omega^2 r^2/c^2(l+kN)^2}(1+\chi_{rkl})\frac{d\delta\Phi_{kl}}{dr}\right]-\frac{(l+kN)^2}{r^2}(1+\chi_{\theta kl})\delta\Phi_{kl}=0 \qquad (1.4)$$

under appropriate boundary conditions. In Eq. (1.4), $\delta\Phi_{kl}$ is proportional to the electric field perturbation, χ_{rkl} and $\chi_{\theta kl}$ are susceptibility functions, ω is the frequency of the perturbation, N is the number of vanes on the anode, the index l with $l = 1, 2,\ldots, N$ designates the azimuthal mode number, and the index k with $k = 0, \pm 1, \ldots$ designates the Floquet mode number.

In principle, solving the eigenvalue problem will allow us to determine the small-signal gain in a magnetron for any given equilibrium electron flow profile. As we will demonstrate in Sec. 3.1, solving the eigenvalue equation in the absence of the electron layer yields a vacuum dispersion relation which agrees with experimental measurements. We plan to solve the eigenvalue problem with the presence of the electron layer and extend the small-gain theory to the relativistic regime.

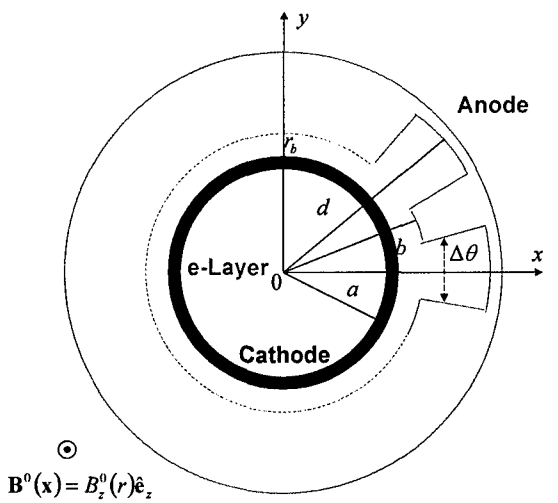

Figure 1.4: Schematic of a multiresonator cylindrical magnetron in a two-dimensional configuration. The cathode is located at $r = a$, whereas the anode is a corrugated slow-wave structure. The electron layer is confined by the applied magnetic field $B_0\hat{e}_z$ (from Chen, 2005).

2. High-Power Klystron Research

In the operation of high-power relativistic klystrons, it is critical to confine the electron beam radially as it becomes sharply bunched along the direction of propagation. Typically, a high-power relativistic klystron employs either a pencil relativistic electron beam or an annular relativistic electron beam.

Under the auspices of the grant (Chen, 2003a), we extended our treatment of the bunched beam confinement from our previous point-charge model (Hess and Chen, 2000 and 2002b, Hess, 2002) to a finite-size bunched beam model (Hess and Chen, 2004), and successfully applied it to improving our understanding of the operational limit of high-power relativistic klystrons (Hess and Chen, 2004). We also explored the possibility of magnetic cusp formation in highly bunched annular beams (Hess and Chen, 2006).

2.1. Determination of the Current Limit on the Confinement of Finite-Size Bunched Pencil Beams in High-Power Relativistic Klystrons (Hess and Chen, 2004)

We derived the space-charge limit for a train of periodic finite-size charged bunches which are slightly displaced from the axis of a circular, perfectly conducting pipe. The general calculation assumed that the bunches, while periodic, may have arbitrary radial and longitudinal density distributions with respect to the beam axis. We obtained results for a few specific distributions, as well as the limits of unbunched and single bunch beams. Finally, we showed how the bunched beam space-charge limit along with the radial rms envelope equation for a bunched beam is applied to predict operational limits of periodic permanent magnet (PPM) focusing klystrons which were designed and tested for Linear Collider (LC).

The results are summarized in Table 2.1 (from Hess and Chen, 2004). Table 2.1 lists the key parameters for the five PPM klystrons (Sprehn, *et al*, 1998; Sprehn, *et al*, 2000; Matsumoto, *et al*, 2001; Chin, *et al*, 2001; SLAC Website http://www-group.slac.stanford.edu/kly/ppm_klystron/ppm_kly.html): operating frequency f, average beam current I_b, beam energy γ_b, the rms magnetic field strength B_{rms}, and the pipe radius a. Table 2.1 also shows the values for $\alpha = 2\pi a/\gamma_b L$ and the experimental space charge (current) parameter $s_{e,exp}$, which can be computed using the formulas $L = \beta_b c/f$ and $N_b = I_b/ef$. The theoretical limit is $s_e/s_e(0,0)$. If the experiment value $s_{e,exp}/s_e(0,0)$ is greater than $s_e/s_e(0,0)$ in a klystron, then substantial beam loss occurs. If the experimental value $s_{e,exp}/s_e(0,0)$ is less than $s_e/s_e(0,0)$ in a klystron, then small beam loss could still occurs due to beam halo formation (Chen and Pakter, 2000; Pakter and Chen, 2000). Our results show good agreement with the experimental observations.

2.2. Exploration of the Possibility of Magnetic Cusp in Highly Bunched Annular Electron Beams in High-Power Klystrons (Hess and Chen, 2006)

We explored the possibility of magnetic cusp formation in high-power klystrons driven by high-intensity annular beams, such as the relativistic klystron oscillator which is currently being studied experimentally at Air Force Research Laboratory.

Table 2.1 Parameters of Several LC PPM Klystrons (from Hess and Chen, 2004)

Parameter	50 MW XL-PPM (SLAC)		50 MW C-Band Toshiba/KEK		75 MW XP-3 (SLAC)
f (GHz)	11.4		5.7		11.4
I_b (A)	190		317		260
γ_b	1.83		1.67		2.00
B_{rms} (T)	0.20		0.17		0.21
a (cm)	0.48		0.90		0.54
α	0.75		0.79		0.74
$s_{e,exp}$	0.19		0.25		0.16
$s_e/s_e(0,0)$	0.90		0.85		0.95
$s_{e,exp}/s_e(0,0)$	0.80		0.8		0.68
Beam Power Loss	0.8%		Small but not measured		~1.0%

For a thin annular disk, the equilibrium force balance equation has the dimensionless form (Hess and Chen, 2006)

$$\frac{\tilde{\omega}^2}{\mu\sqrt{1-\tilde{r}^2\tilde{\omega}^2}} = \tilde{\omega} - \frac{\lambda}{\tilde{r}}\sum_{m=1}^{\infty}\tilde{\sigma}_m J_1(j_{0m}\tilde{r})\coth[\pi j_{0m}/\alpha]$$
$$-\lambda\tilde{\omega}\left\{\sum_{m=1}^{\infty}\tilde{\kappa}_m J_0(j_{0m}\tilde{r})\coth[\pi j_{0m}/\alpha] - \frac{2\alpha}{\pi}\sum_{m=1}^{\infty}\frac{\tilde{\kappa}_m J_1(j_{0m})}{j_{0m}^2}\right. \qquad (2.1)$$
$$\left. -\frac{2\alpha^2}{\pi}\sum_{m=1}^{\infty}\sum_{n=1}^{\infty}\frac{\tilde{\kappa}_m n J_1(j_{0m})}{j_{0m}^2+n^2\alpha^2}\frac{I_0(n\alpha\tilde{r})}{I_1(n\alpha)}\right\},$$

where $\omega(r) \equiv V_\theta^{rest}(r)/r$, $\tilde{\omega} = \omega a/c$, $\tilde{\sigma} = \sigma\pi a^2$, $\tilde{\kappa} = \kappa\pi a^2/c$, $\mu = \omega_c a/c$, $\lambda = 2N_b e^2/m_e c\omega_c a^2$, and $\omega_c = eB_0/m_e c$. Equation (2.2.1) predicted the formation of a magnet cusp as the beam current is increased, as shown in Fig. 2.2.1.

Figure 2.1 shows plots of $a\omega/c$ and B^{self}/B_0 vs. r/a for $\mu = 10.7$ and two cases of $\lambda = 0.05$ and $\lambda = 0.1115$. The surface number density profile is chosen as

$$\sigma(r) = \begin{cases} 0, & r \le r_i, \\ 3(r_o - r)(r - r_i)/\pi\bar{r}\delta^3, & r_i \le r \le r_o, \\ 0, & r_o \le r, \end{cases} \qquad (2.2)$$

where $\bar{r} = (r_o + r_i)/2 = 0.8a$ is an average beam radius and $\delta = r_o - r_i = 0.2a$ is the beam width. Notice that as λ increases to a critical value $\lambda_{cusp} \cong 0.1116$, $B^{self}(\tilde{r})/B_0$ forms a

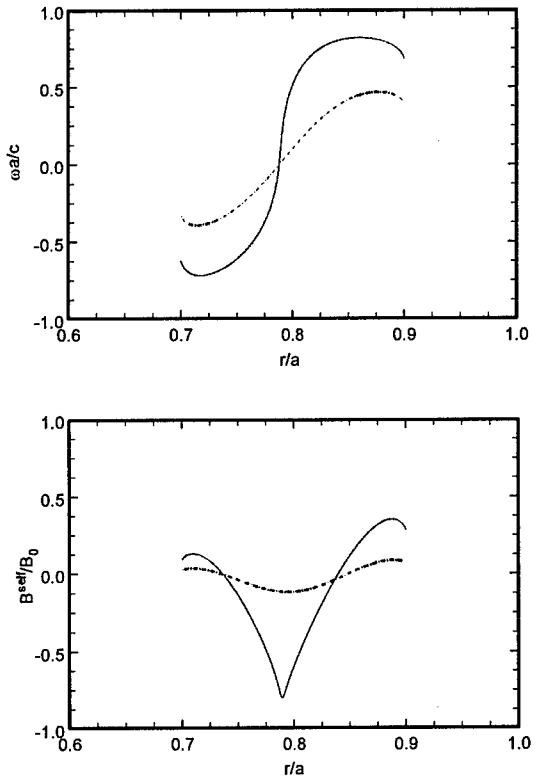

Figure 2.1: Plots of (top) $a\omega/c$ and B^{self}/B_0 vs. r/a predicted by Eq. (2.1) for $\mu = 10.7$ and two cases of $\lambda = 0.05$ and $\lambda = 0.1115$, using the surface density profile defined in Eq. (2.2) (from Hess and Chen, 2006).

cusp shape at a specific point $r^* \cong 0.7881$, with $B^{self}(\tilde{r}^*)/B_0 = -1$. Near the cusp, we found numerically that the magnetic field scales approximately as $B^{self}(r) + B_0 \propto (r^* - r)^{\alpha_1}$ with $\alpha_1 \cong 0.5$ for $r < r^*$, and $B^{self}(r) + B_0 \propto (r - r^*)^{\alpha_2}$ with $\alpha_2 \cong 0.73$ for $r > r^*$. Beyond the cusp with $\lambda > \lambda_{cusp}$, we were unable to find numerical solutions to the equilibrium momentum equation.

The physics of magnetic cusp formation is that as the beam current increases, the rotation of the electron flow becomes relativistic and produces a diamagnetic field which conceals the applied magnetic field.

While magnetic cusp formation is a new phenomenon predicted by our theory, it remains to be seen whether such phenomena can be observed in annular-beam driven klystron experiments. A key question would be whether the electrons will be sufficiently bunched along the direction of beam propagation, which will be a subject of our future investigations.

3. Development of Ellipse-Shaped Ribbon-Beam Theory for High-Power Microwave Device Applications

Existing HPM devices employ either a pencil electron beam or an annular electron beam. One of the main objectives in high-power microwave (HPM) research is to develop innovative science and technology which could lead to improve the efficiency, output power level, and other performance (such as weight reduction) of high-power microwave (HPM) devices.

A promising approach is to use a large-aspect-ratio ellipse-shaped electron beam rather than the conventional pencil or annular electron beam as the energy source. Compared with a conventional HPM device, a HPM device powered by an ellipse-shaped electron beam has the following attractive features:

a) Power scales as f^{-1} instead of f^{-2} (where f is the frequency), thus more power;
b) Low effective beam perveance, thus higher efficiency;
c) Use of permanent magnets for beam focusing, thus lower energy consumption; and
d) Low cathode loading, thus longer device lifetime.

However, there was lack of a fundamental understanding of the generation (or formation) of high-power ellipse-shape electron beam. Indeed, few analytic results were available until the breakthrough we made recently in the development of three-dimensional theory and three-dimensional simulation of the generation (or formation) of ellipse-shaped ribbon electron beams.

The formation and transport of ribbon (sheet) electron beams, which is three-dimensional in nature, had presented major challenges in the realization of ribbon-beam microwave devices. Under the auspices of the present grant (Chen, 2003a), we made major breakthroughs in the theoretical understanding of ribbon-beam formation and transport.

3.1. Theory of Elliptic Beam Formation (Bhatt and Chen, 2005; Bhatt, Bemis and Chen, 2005 and 2006)

We published an important paper on a three-dimensional theory of non-relativistic, laminar, elliptic beam formation (Bhatt and Chen, 2005). The beam was shown to have the Child-Langmuir form (Bhatt and Chen, 2005). An analytic expression for the electrostatic potential outside the beam was derived. Equipotentials corresponding to electrode surfaces were computed numerically. The effectiveness of the electric field formed by the electrodes in focusing and preserving the elliptic Child-Langmuir beam was verified via 3D ray-tracing simulations.

Figure 3.1 shows a schematic of an elliptic beam and the elliptical coordinate system used in our theory. Figure 3.2 shows the contours of the potentials for the cathode and anode focusing electrodes. Figure 3.3 shows the OMNITRAK simulation of the laminar flow electron trajectories for the case shown in Fig. 3.2. The elliptic beam shown in Figs. 3.2 and 3.3 has an aspect ratio of 10:1.

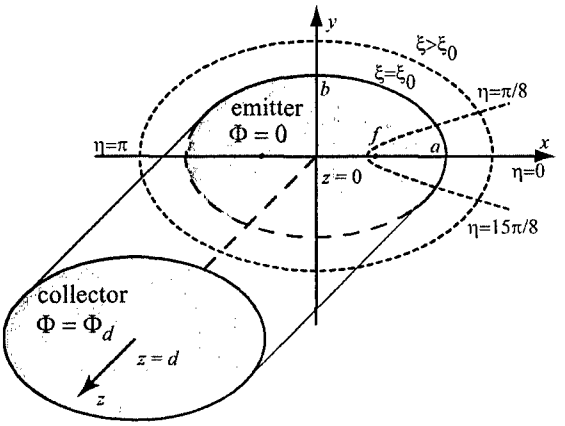

Figure 3.1: Schematic of an elliptic electron diode and elliptical coordinate system (from Bhatt and Chen, 2005).

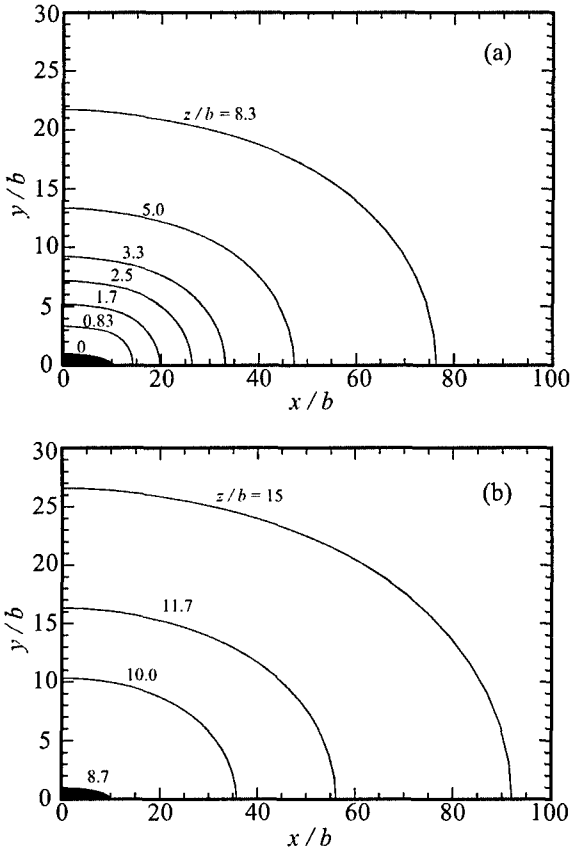

Figure 3.2: Potential contours at (a) cathode and (b) anode focusing electrodes (from Bhatt and Chen, 2005).

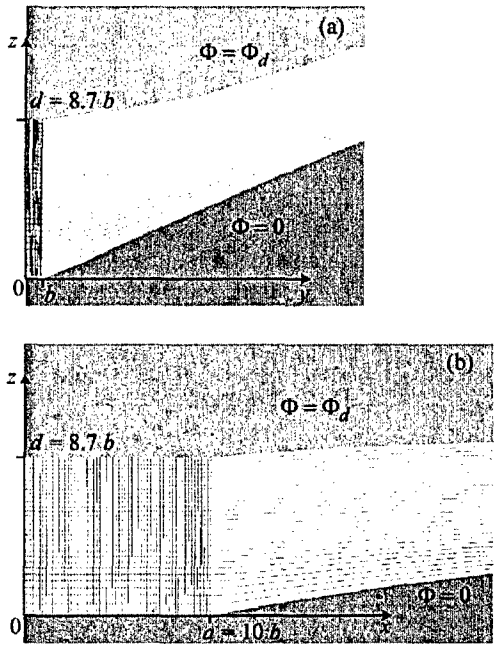

Figure 3.3: Laminar flow electron trajectories from a 3D OmniTrak simulation projected to (a) vertical plane (y,z) and (b) horizontal plane (x,z) (from Bhatt and Chen, 2005).

The treatment was extended (Bhatt, Bemis and Chen, 2005 and 2006) to consider whether the diode geometry solutions thus obtained are robust to perturbations and limitations of the sort likely to be encountered in a realistic device: finite extent, part misalignment, tolerances for mechanical and thermal stresses, etc. Analytic and semi-analytic estimates were obtained along with simulations utilizing the 3D trajectory code, OMNITRAK. It was found that the elliptic-beam solution is quite stable and robust, and its desirable properties can be maintained in a realistic diode.

For his joint paper "Three-Dimensional Theory and Simulation of Large-Aspect-Ratio Ellipse-Shaped Charged-Particle Beam Gun" with Tom Bemis and Chiping Chen (2005), our graduate student Mr. Ronak Bhatt received *First-Place Award for an Outstanding Technical Paper by Student* at Particle Accelerator Conference, May 16-20, 2005, which over 1000 scientists from all over the world attended. Mr. Bhatt also presented an invited paper at ICOPS 2005, Monterey, CA (Bhatt, Bemis and Chen, 2005).

3.2. Theory of Elliptic Beam Focusing and Transport (Zhou, Bhatt and Chen, 2006)

For HPM devices, the transport and focusing of an ellipse-shaped electron beam is another important area which requires research and development. Under the auspices of the current research, we showed that there exists an exact paraxial cold-fluid equilibrium of a high-intensity, space-charge-dominated charged-particle beam with a periodically twisted elliptic cross section in a non-axisymmetric periodic magnetic field. Generalized envelope equations, which determine the beam envelopes, ellipse orientation, density, and internal flow velocity profiles, were derived. Nonrelativistic and relativistic examples of such beam equilibria were discussed. The equilibrium and stability of such beams were demonstrated by self-consistent particle-in-cell (PIC) simulations.

Our theory (Zhou, Bhatt and Chen, 2006) describes a high-intensity, space-charge-dominated unbunched beam, in which kinetic (emittance) effects are negligibly small. The focusing field is a three-dimensional (3D) non-axisymmetric periodic magnetic field which can be described in the paraxial approximation as

$$\mathbf{B}^{ext}(\mathbf{x}) \approx B_0\left[\frac{k_{0x}^2}{k_0}\cos(k_0 s)x\hat{\mathbf{e}}_x + \frac{k_{0y}^2}{k_0}\cos(k_0 s)y\hat{\mathbf{e}}_y - \sin(k_0 s)\hat{\mathbf{e}}_z\right], \tag{3.1}$$

where $k_0 = 2\pi/S$, $k_{0x}^2 + k_{0y}^2 = k_0^2$, and S is the axial periodicity length. The 3D magnetic field in Eq. (2.3.1) is fully specified by the three parameters B_0, S and k_{0x}/k_{0y}. The cold-fluid equilibrium equations in the paraxial approximation are (Zhou, Bhatt and Chen 2005):

$$\beta_b c\frac{\partial}{\partial s} + \nabla_\perp \cdot (n_b \mathbf{V}_\perp) = 0, \tag{3.2}$$

$$n_b\left(\beta_b c\frac{\partial}{\partial s} + \mathbf{V}_\perp \cdot \frac{\partial}{\partial \mathbf{X}_\perp}\right)\mathbf{V}_\perp = \frac{qn_b}{\gamma_b m}\left[-\frac{1}{\gamma_b^2}\nabla_\perp \phi^s + \beta_b \hat{\mathbf{e}}_z \times \mathbf{B}_\perp^{ext} + \frac{\mathbf{V}_\perp}{c} \times B_z^{ext}(s)\hat{\mathbf{e}}_z\right], \tag{3.3}$$

$$\nabla_\perp^2 \phi^s = \beta_b^{-1}\nabla_\perp^2 A_z^2 = -4\pi q n_b, \tag{3.4}$$

which are nonlinear.

The beam can be adequately described by cold-fluid equations since the kinetic effects are negligibly small in the beam that we are considering. We find that a well confined unbunched beam exists in such a focusing system. Inside the ellipse-shaped beam boundary, the beam has the uniform density profile

$$n_b(\mathbf{x}_\perp, s) = \frac{N_b}{\pi a(s) b(s)}\Theta\left[1 - \frac{\tilde{x}^2}{a^2(s)} - \frac{\tilde{y}^2}{b^2(s)}\right] \tag{3.5}$$

and the linear flow velocity profile

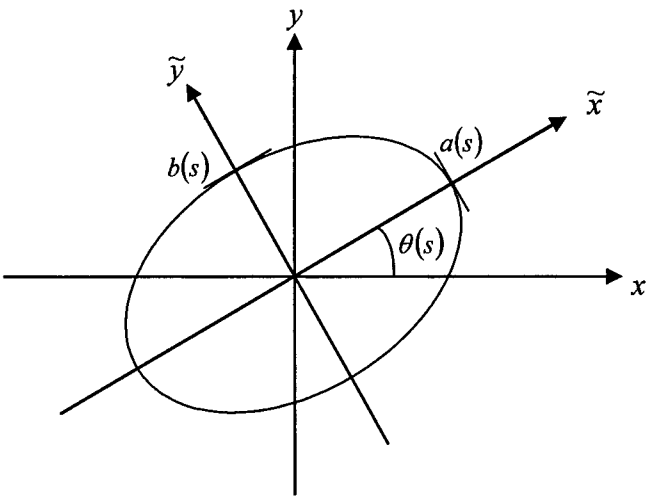

Figure 3.4: Untwisted and twisted coordinate systems (from Zhou, Bhatt and Chen, 2006).

$$\mathbf{V}_\perp(\mathbf{x}_\perp, s) = \left[\mu_x(s)\tilde{x} - \alpha_x(s)\tilde{y}\right]\beta_b c\hat{\mathbf{e}}_{\tilde{x}} + \left[\mu_y(s)\tilde{y} + \alpha_y(s)\tilde{x}\right]\beta_b c\hat{\mathbf{e}}_{\tilde{y}}, \qquad (3.6)$$

where $\mathbf{x}_\perp = \tilde{x}\hat{\mathbf{e}}_{\tilde{x}} + \tilde{y}\hat{\mathbf{e}}_{\tilde{y}}$ is a transverse displacement in the twisted coordinate system illustrated in Fig. 3.4; $\theta(s)$ is the twist angle of the ellipse; $\Theta(x) = 1$ if $x > 0$ and $\Theta(x) = 0$ if $x < 0$.

It can be shown that both the equilibrium continuity equation and force equation are satisfied if the dynamical variables $a(s)$, $b(s)$, $\mu_x(s) \equiv a^{-1}da/ds$, $\mu_y(s) \equiv b^{-1}db/ds$, $\alpha_x(s)$, $\alpha_y(s)$ and $\theta(s)$ obey the generalized beam envelope equations (Zhou, Bhatt and Chen, 2006)

$$\frac{d^2a}{ds^2} - \left[\frac{b^2\left(\alpha_x^2 - 2\alpha_x\alpha_y\right) + a^2\alpha_y^2}{a^2 - b^2} + \sqrt{\kappa_{z0}}\frac{k_{0x}^2 - k_{0y}^2}{k_0}\cos(k_0 s)\sin(2\theta) - 2\sqrt{\kappa_{z0}}\alpha_y\sin(k_0 s)\right]a - \frac{2K}{a+b} = 0, \qquad (3.7)$$

$$\frac{d^2b}{ds^2} + \left[\frac{a^2\left(\alpha_y^2 - 2\alpha_x\alpha_y\right) + b^2\alpha_x^2}{a^2 - b^2} + \sqrt{\kappa_{z0}}\frac{k_{0x}^2 - k_{0y}^2}{k_0}\cos(k_0 s)\sin(2\theta) + 2\sqrt{\kappa_{z0}}\alpha_x\sin(k_0 s)\right]b - \frac{2K}{a+b} = 0, \qquad (3.8)$$

$$\frac{d}{ds}\left(a^2\alpha_y\right) - \frac{ab^3\left(\alpha_x - \alpha_y\right)}{a^2 - b^2}\frac{d}{ds}\left(\frac{a}{b}\right) - 2\sqrt{\kappa_{z0}}\cos(k_0 s)\frac{k_{0x}^2\cos^2\theta + k_{0y}^2\sin^2\theta}{k_0}a^2 - 2\sqrt{\kappa_{z0}}a\frac{da}{ds}\sin(k_0 s) = 0, \qquad (3.9)$$

$$\frac{d}{ds}\left(b^2\alpha_x\right) - \frac{a^3b\left(\alpha_x - \alpha_y\right)}{a^2 - b^2}\frac{d}{ds}\left(\frac{b}{a}\right) - 2\sqrt{\kappa_{z0}}\cos(k_0 s)\frac{k_{0x}^2\sin^2\theta + k_{0y}^2\cos^2\theta}{k_0}b^2 - 2\sqrt{\kappa_{z0}}b\frac{db}{ds}\sin(k_0 s) = 0, \qquad (3.10)$$

$$\frac{d\theta}{ds} = \frac{a^2\alpha_y - b^2\alpha_x}{a^2 - b^2}, \qquad (3.11)$$

where $\sqrt{\kappa_{z0}} \equiv qB_0/2\gamma_b\beta_b mc^2$ and $K \equiv 2q^2N_b/\gamma_b^3\beta_b^3 mc^2$.

Table 3.1 System parameters for elliptic-beam examples

Parameter	Nonrelativistic (RBA)	Mildly Relativistic (RBA)	Fully Relativistic (RBK)	Fully Relativistic (RBK)
Application	Wireless Communication	Missile Defense	International Linear Collider	Directed Energy
Frequency (GHz)	1.95	2.8	1.3	1.3
RF Power (kW)	0.2 (cw)	500 (pulsed)	10,000 (pulsed)	200,000 (pulsed)
Current (A)	0.11	18.5	85.5	450
Voltage (kV)	2.29	45.0	198.5	600
S (cm)	1.912	2.626	2.2	3.5
k0x/k0y	1.60	1.44	1.52	1.51
B0 (kG)	0.337	1.099	2.40	2.50
a/b	6.0	4.0	5.0	5.0
a (cm)	0.373	0.585	0.425	0.663
θ_{max} (deg)	10.4	11.5	8.8	7.2

A numerical module in the MIT 2D Periodically Focused Beam (PFB2D) code was developed to solve the generalized envelope equations (3.7)-(3.11). The matched solution was determined with Newton's method. The beam equilibria predicted by the generalized envelope equations were verified by 2D particle-in-cell (PIC) simulations using the PFB2D code. In the PFB2D simulations, we used the paraxial field in Eq. (3.1), typically 5×10^5 particles, a square grid with 400×400 cells, and a square conducting pipe with a full width which is 3 times the semi major axis of the beam.

As an example, we have considered a relativistic ribbon beam with voltage $V_b = 198.5$ keV, current $I_b = 85.5$ A, aspect ratio $a/b = 5$, and non-axisymmetric periodic permanent magnet focusing with $B_0 = 2.4$ kG, $S = 2.2$ cm, and $k_{0y}/k_{0x} = 1.52$ (see Table 3.1, Column 4). We propose to use it in a 10 MW L-Band ribbon-beam klystron (RBK) for a linear collider (LC).

For such a system the matched solution of the generalized envelope equations is calculated numerically as shown in Figs. 3.5(a)-(c) with the corresponding parameters: $k_{0x} = 1.57$ cm^{-1}, $k_{0y} = 2.39$ cm^{-1}, $\sqrt{\kappa_{z0}} = 0.732$ cm^{-1}, and $K = 1.13\times10^{-2}$. The solution to the generalized envelope equations shows that the semiaxes of the elliptical beam remain roughly constant with small oscillations, that the orientation of the ellipse twists periodically with an amplitude of ten degrees, and that the normalized rotation flow velocities α_x and α_y oscillate with the magnet periodicity. Shown in Figs. 3.5(a) and 3.5(b), the dotted curves are the envelopes and angle of the beam ellipse obtained from the PFB2D simulation. It is worthwhile pointing out that the normalized velocities μ_x, μ_y, α_x and α_y vanish at $s = 0$ which makes it a natural matching point for a parallel-flow beam with negligibly small emittance (Bhatt and Chen, 2005).

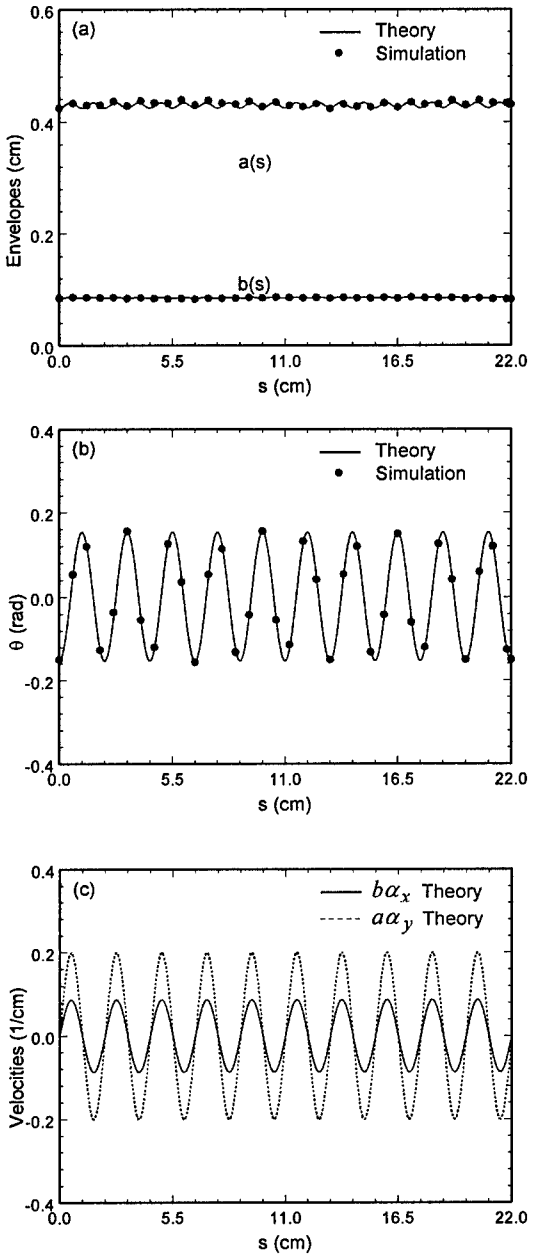

Figure 3.5: Plots of (a) envelopes $a(s)$ and $b(s)$, (b) twist angle $\theta(s)$, and (c) normalized rotational velocities $b(s)\alpha_x(s)$ and $a(s)\alpha_y(s)$ versus the axial distance s for the relativistic twisted ellipse-shaped beam in Table 3.1, Column 4. The solid and dashed curves are the generalized envelope solution, whereas the dotted curves are from the PFB2D simulation.

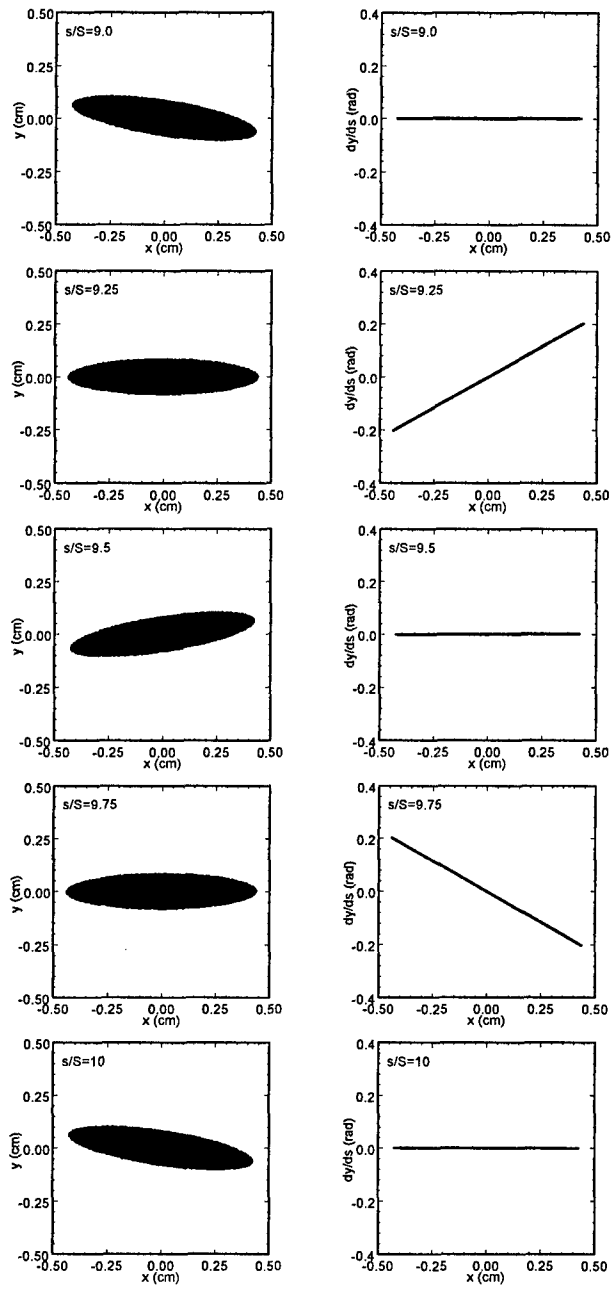

Figure 3.6 Plots of 10,000 particles (a sample of the 5×10^5 particles in the PFB2D simulation) in the (x, y) plane and $(x, dy/ds)$ plane for five snapshots within one period: $s/S = 9.0, 9.25, 9.5, 9.75$ and 10.0 for the same beam shown in Fig. 3.5.

The PFB2D simulation also shows that the transverse beam distribution preserves the equilibrium profile as it propagates. In Fig. 3.6, 10,000 particles (a sample of the 5×10^5 particles in the PFB2D simulation) are plotted in the (x,y) plane and $(x,dy/ds)$ plane for five snapshots within one period: $s/S = 9.0, 9.25, 9.5, 9.75$ and 10.0 for the same beam shown in Fig. 3.5. This also suggests that the beam equilibrium is stable, although we have not done a full stability analysis of the beam equilibrium.

These high-intensity twisted elliptic beam equilibria exist over a wide region of parameters ranging from the nonrelativistic to relativistic regimes. In addition to the relativistic elliptic beam equilibrium for discussed in Figs. 2.3.5 and 2.3.6, we present three additional examples in Table 2.3.1 for ribbon-beam microwave devices which have applications ranging from wireless communications, to high-power radar (e.g., AEGIS radar), and to directed energy.

3.3. Spin-off of Ribbon-Beam Technology for Commercial, Defense and Scientific Applications

We are spinning off the ribbon-beam technology to Beam Power Technology, Inc., a high-tech start-up company whose mission is to apply it in commercial, defense, and scientific applications. The nonrelativistic elliptic beam corresponds to a beam design for a high-efficiency 200 W ribbon-beam amplifier (RBA) which is being developed at Massachusetts Institute of Technology (MIT) for communication, whereas the mildly relativistic elliptic beam is proposed for a high-power, high-efficiency RBA for radar applications. The two relativistic elliptic beams are proposed for International Linear Collider (ILC) and direct energy application, respectively.

4. Chaotic Particle Motion and Halo Formation in Small Aperture Systems (Zhou and Chen, 2005)

It is important to identify the mechanisms of chaotic particle motion, beam halo formation, and beam loss, and to develop techniques to control them in particle beam devices in general and HPM devices in particular. Under the auspices of the present grant, we carried out a parametric study of chaotic particle motion, beam halo formation, and beam loss in an intense charged-particle beam in a small-aperture alternating-gradient focusing system (Zhou and Chen, 2005). The mechanism for chaotic particle motion, beam halo formation, and/or beam loss is due to the image charge effects of a pulsating elliptic beam in a small-aperture circular conducting pipe.

Figure 4.1 shows a Poincaré surface-of section plot for the trajectories of 100 test particles for propagation over 400 lattice periods in the phase plane (x,y) with normalized pipe radius $\hat{R} = R/a = 4.0$, where a is the maximum value of the semi major axis of the pulsating elliptic beam. The system parameters are chosen to be $\eta = 0.5$, $KS/\varepsilon_x = 10.0$, $\varepsilon_x = \varepsilon_y = \varepsilon$, and $\sigma_v = 80°$. In. Fig. 4.1, the scattered particles are chaotic. They form a halo which extends to the circular conductor wall, permitting particles to strike the wall.

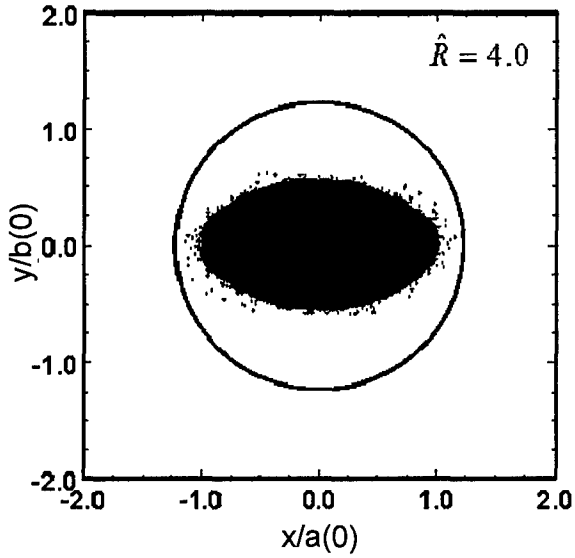

Figure 4.1: Poincaré surface-of section plot for the trajectories of 100 test particles for propagation over 400 lattice periods in the phase plane (x, y) with the system parameters $\hat{R} = R/a = 4.0$, $\eta = 0.5$, $KS/\varepsilon_x = 10.0$, $\varepsilon_x = \varepsilon_y = \varepsilon$, and $\sigma_v = 80°$ (from Zhou and Chen, 2005).

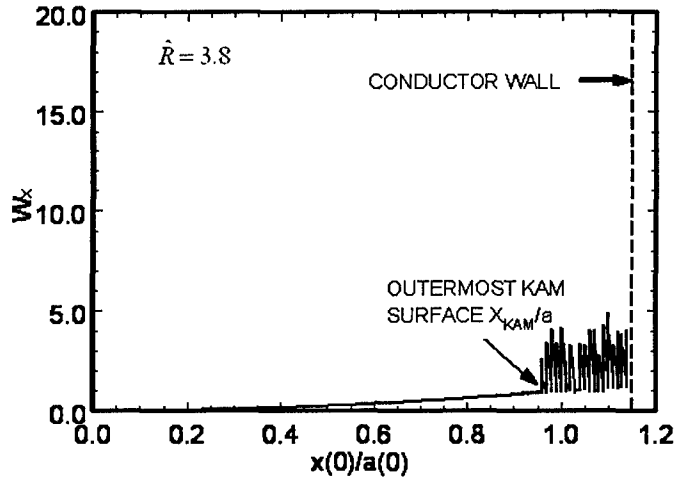

Figure 4.2: Plot of the range of the transverse energy W_x for test particles propagating over 2000 lattice periods for $\hat{R} = 3.8$, $\eta = 0.5$, $KS/\varepsilon_x = 10.0$, $\varepsilon_x = \varepsilon_y = \varepsilon$, and $\sigma_v = 80°$. The 115 test particles are loaded uniformly at $s = 0$ between the interval $0 \le W_x \le 1.15$ along the x' axis in phase space (from Zhou and Chen, 2005).

A more detailed description of how such chaotic particle motion arises is illustrated in Fig. 4.2, which shows a plot of the range of the transverse energy W_x for test particles propagating over 2000 lattice periods for $\hat{R} = 3.8$, $\eta = 0.5$, $KS/\varepsilon_x = 10.0$, $\varepsilon_x = \varepsilon_y = \varepsilon$, and $\sigma_v = 80°$. The 115 test particles are loaded uniformly at $s = 0$ between the interval $0 \le W_x \le 1.15$ along the x' axis in phase space.

In designing on an elliptic electron beam for HPM device applications, it is important to understand image charge effects and determine the parameter space where the image charge effects are negligibly small. This will be an important area of future research.

5. Research Initiative on Relativistic Electron Diodes and Beams for HPM Device Applications

In a HPM device, a relativistic diode is used to generate a high-power electron beam which interacts with rf structure to generate intense electromagnetic waves. The performance of a HPM device, in general, depends strongly on how well the relativistic electron diode and subsequent beam system are design. Despite of decades of theoretical and experimental research on HPM devices, our understanding of relativistic electron diodes and beams is limited. To date, relativistic gun design relies on computer simulations.

A major problem in a typical circular relativistic electron gun is that the beam density fluctuates as it propagates in the focusing magnetic field. The density fluctuations cause undesirable effects such as beam mismatch (or beam scalloping), emittance growth, and beam halo formation, all of which degrade the performance of HPM sources using such beam.

We have taken an initiative to develop the equilibrium theory of axisymmetric $(\partial/\partial\theta = 0)$ relativistic electron diodes and beams for HPM device applications. In particular, we have formulated the relativistic electron beam generation and propagation problem. By introducing the electron flow and magnetic flux surfaces $\chi = rB_\theta$ and $\psi = rA_\theta$, respectively, where $\mathbf{B} = \nabla \times \mathbf{A}$ is the total magnetic field and $\mathbf{A}$ is the vector potential. The energy conservation along flow lines is expressed as

$$\gamma mc^2 - e\phi = \varepsilon(\chi), \tag{5.1}$$

where $-e$ is the electron charge, ϕ is the electrostatic potential, and γ is the relativistic mass factor. The azimuthal angular momentum conservation is expressed as

$$rm\gamma V_\theta - \frac{e}{c}\psi = L(\chi). \tag{5.2}$$

It can be shown that the problem of relativistic electron diodes and beams is fully described by (Stowell and Chen, 2005)

$$\nabla^2\phi = 4\pi en, \tag{5.3}$$

$$\Delta^* \psi = 4\pi e r n \frac{V_\theta}{c}, \tag{5.4}$$

$$\frac{\gamma c^2}{(4\pi e n r)^2} \nabla\chi \cdot \left([(\nabla\chi \times \hat{\mathbf{e}}_\theta) \cdot \nabla](\nabla\chi \times \hat{\mathbf{e}}_\theta) \right) = \frac{e}{m} \left(\nabla\chi \cdot \nabla\phi - \frac{\chi |\nabla\chi|^2}{4\pi e n r^2} - \frac{V_\theta}{cr} \nabla\chi \cdot \nabla\psi \right), \tag{5.5}$$

where $\Delta^* = r \frac{\partial}{\partial r} \frac{1}{r} \frac{\partial}{\partial r} + \frac{\partial^2}{\partial z^2}$ and $\mathbf{V} = -\frac{c}{4\pi e n} \nabla\chi \times \frac{\hat{\mathbf{e}}_\theta}{r} + V_\theta \hat{\mathbf{e}}_\theta$. Equations (5.1)-(5.5) provide a general description of axisymmetric relativistic electron diodes and beams. Solving them will yield various equilibria for relativistic electron diodes and beams, which will be our future investigations.

6. References

Bhatt, R. and C. Chen, 2003, "Laminar electron flow solutions for two-dimensional electrode geometries," American Physical Society, Bulletin **48**, 314.

Bhatt, R. and C. Chen, 2004, Research notes "Two-dimensional stead-state charged fluid flow," unpublished.

Bhatt, R. and C. Chen, 2005, "Theory and Simulation of Non-Relativistic Elliptic Beam Formation with Child-Langmuir Flow Characteristics," Phys. Rev. ST Accel. Beams **8**, 014201.

Bhatt, R. T. Bemis, and C. Chen, 2005, "Three-Dimensional Theory and Simulation of Large-Aspect-Ratio Ellipse-Shaped Charged-Particle Beam Gun," Proceedings of 2005 Particle Accelerator Conference, p. 3372 (**First Prize for Outstanding Technical Paper by a Student**).

Bhatt, R. T. Bemis, and C. Chen, 2006, "Three Dimensional Theory and Simulation of Non-Relativistic Elliptic Electron and Ion Beam Generation" (**Invited Paper**) IEEE Trans. Plasma Sci. **34**, 187.

Bosman, H.L., et al., 2005, American Physical Society, Bulletin **50**, 72.

Cartwright, K., 2005, private communication.

Chen, C., 2003, "Coherent structures and chaos control in high-power microwave devices" Research proposal funded by AFOSR under Grant No. F49620-03-1-0230, Chiping Chen, Principal Investigator; and references therein.

Chen, C., 2004, "Analytic results on high-power microwave devices," presented at AFRL Magnetron/PIC Simulation Workshop, May 2-3.

Chen, C., 2005, Research notes "Small-signal theory of magnetrons," unpublished.

Chen, C. R. Pakter, and R.C. Davidson, 1997, Phys. Rev. Lett. **79**, 225.

Chen C., and R. Pakter, 2000, "Mechanisms and control of beam halo formation in Intense microwave sources and accelerators," (**Invited Paper**), Phys. Plasmas **7**, 2203.

Chin, Y.H., *et al*, 2001, Proceedings of the 2001 Particle Accelerator Conference, edited by P. W. Lucas and S. Webber, p. 3792.

Davidson, R. C., H. W. Chan, C. Chen and S. Lund, 1991, Rev. Mod. Phys. **63**, 73.

Davies, J.A., and C. Chen, 2006, "Vortex structures in high density non-axisymmetric $\mathbf{E} \times \mathbf{B}$ equilibrium flow," Phys. Plasmas **13**, 012310.

Hess, M., 2002, "Green's Function Analysis of Bunched Charge-Particle Beams" (Ph.D. Dissertation, Massachusetts Institute of Technology), May 17.

Hess, H., and C. Chen, 2000, "Confinement criterion for a highly bunched beam," Phys. Plasma **7**, 5206.

Hess, M., and C. Chen, 2001, "Bunched annular beam equilibrium and confinement," in *Intense Microwave Pulses VIII*, edited by H. E. Brandt, SPIE Proc. **4371**, 57.

Hess, M., and C. Chen, 2002a, "Equilibrium and confinement of bunched annular beams," Phys. Plasmas **9**, 1442.

Hess, M., and C. Chen, 2002b "Beam confinement in high-power periodic permanent magnet focusing klystrons," Phys. Lett. **A295**, 305.

Hess, M., and C. Chen, 2004, "Space-charge limit in a finite-size bunched charged-particle beam in a circular conducting pipe," Phys. Rev. ST, Accel. Beams **7**, 092002.

Hess, M., and C. Chen, 2006, "Formation of a self-magnetic field cusp in highly bunched relativistic annular electron beam," Phys. Plasmas **13**, 053108.

Kaup, D.J., 2005, "Drift resonances in high-density neuneutral plasmas," manuscript.

Matsumoto, H., *et al*, 2001, Proceedings of the 2001 Particle Accelerator Conference, edited by P. W. Lucas and S. Webber, p. 993.

Pakter, R., and C. Chen, 2000, "Electron beam halo formation in periodic permanent focusing klystron amplifiers," IEEE Trans. Plasma Sci., **28**, 502.

Riyopoulos, S., Phys. Rev. Lett. **81**, 3026.

Sprehn, D., G. Caryotakis, E. Jongewaard, and R. M. Phillips, 1998, "Periodic permanent magnetic development for linear collider X-band klystrons," Proc. XIX International Linac Conf. (Argonne National Laboratory Report ANL-98/28), p. 689.

Sprehn, D., G. Caryotakis, E. Jongewaard, R. M. Phillips, and A. Vlieks, 2000, "X-band Klystron development at the Stanford Linear Accelerator Center," in *Intense Microwave Pulses VII*, edited by H. E. Brandt, SPIE Proc. **4031**, 132.

Stowell, R.H. and C. Chen. 2005a, "Exact Analytical Solutions for Relativstic Parapotential Flow with Spatially Varying Total Energy," American Physical Society, Bulletin **48**, 47.

Stowell, R.H. and C. Chen, 2005b, Research notes "Relativistic Electron Flow," unpublished.

Yamamoto, K., H. Kuronuma, T. Koinuma, and N. Tashino, 1987, IEEE Trans. Electron Dev. **ED-34**, 1223.

Zhou, J., and C. Chen, 2005, "Parametric studies of image charge effects on an intense charged-particle beam in a small-aperture alternating-gradient focusing system," Nucl. Inst. Methods. Phys. Res. **A544**, 492.

Zhou, J., R. Bhatt, C. Chen, 2006, "Cold-Fluid Theory of Equilibrium and Stability of a High-Intensity Periodically Twisted Ellipse-Shaped Charged-Particle Beam," Phys. Rev. ST-AB 9, 034401.